Effects of translational coupling on dissipative localized states

F. del Campo,[1] F. Haudin,[2] R. G. Rojas,[3] U. Bortolozzo,[2] M. G. Clerc,[1] and S. Residori[2]
[1]*Departamento de Física, Facultad de Ciencias Físicas y Matemáticas, Universidad de Chile, Casilla 487-3, Santiago Chile*
[2]*Institut Nonlinéaire de Nice, Université de Nice-Sophia Antipolis, Centre National de la Recherche Scientifique, 1361 route des Lucioles 06560 Valbonne, France*
[3]*Instituto de Física, Pontificia Universidad Católica de Valparaíso, Casilla 4059, Valparaíso, Chile*
(Received 30 March 2012; published 4 September 2012)

Nonequilibrium localized states under the influence of translational coupling are studied experimentally and theoretically. We show that localized structures are deformed and advected in the direction of the coupling, thus undergoing different instabilities. Experimentally, localized structures are obtained in a light valve with optical feedback. By introducing a tilt of one mirror in the feedback loop, localized structures acquire a translational coupling. To understand the phenomenon in a universal framework we consider a prototypical model of localized states with translational coupling in one and two spatial dimensions. The model allows us to analytically characterize the propagation speed and the deformation exhibited by the localized state profiles as well as to figure out different mechanisms of destabilization of these dissipative structures. The results are in good qualitative agreement with the experimental and numerical observations.

DOI: 10.1103/PhysRevE.86.036201 PACS number(s): 05.45.−a, 42.65.−k, 45.70.Qj

I. INTRODUCTION

Nonequilibrium systems, that is, systems with injection and dissipation of energy, are characterized by exhibiting a spontaneous self-structuration in response to the optimization of energy transport [1–3]. Emerging particle-type solutions in macroscopic dissipative systems, also known as localized states or localized structures (LSs), have been observed in different physical contexts such as domains in magnetic materials, chiral bubbles in liquid crystals, current filaments in gas discharge, spots in chemical reactions, localized states in fluid surface waves, oscillons in granular media, isolated states in thermal convection, solitary waves in nonlinear optics, and surface solitons in magnetic fluids (see the reviews in Refs. [4–6] and references therein). These observations give evidence of the universality of these dissipative localized states. Although such states are spatially extended, they exhibit properties typically related to particles. Indeed, one can characterize them as a family of continuous parameters such as position, amplitude, and width. This is the type of description and strategy used in physical theories such as quantum mechanics and particle physics. Localized states emerging in extended dissipative systems are composed of a large number of constituents that behave coherently. Solitons, such as those reported in fluid dynamics, nonlinear optics, and Hamiltonian systems [7,8], are the paradigmatic example of a macroscopic localized state. These solitons arise from a robust balance between dispersion and nonlinearity. The generalization of this concept to dissipative and out of equilibrium systems has led to several studies in the past few decades, in particular to the definition of *localized structures* intended as patterns appearing in a restricted region of space [2,3].

An adequate theoretical description of dissipative localized states has been established in one-dimensional spatial systems based on spatial trajectories connecting a steady state with itself. Then localized states arise as homoclinic orbits from the viewpoint of dynamical systems theory (see the review in Ref. [9] and references therein). Localized patterns can be understood as homoclinic orbits in the Poincaré section of the corresponding spatial-reversible dynamical system [9–13]. They can also be understood as a consequence of the front interaction with oscillatory tails [14,15]. There is another type of stabilization mechanism that generates LSs without oscillatory tails based on nonvariational effects [16], where front interaction is led by the nonvariational terms [17].

One of the great interests in studying these LSs is their potential use as information storage units, in other words, optical bits [18]. Thus it is relevant to develop control and manipulation methods of localized states. Different methods have been proposed to achieve such control, for example, by applying spatial forcing [19–22]. Another possibility is to induce gradients to the localized state, for example, through the use of a phase or amplitude gradient, which produces drift on dissipative localized structures [23], as well as on cavity solitons [24], or by tilting a vertically driven channel with water generating motion in a hydrodynamic soliton [25]. Alternatively, one can generate motion of the localized state by introducing a delay in the feedback that induces spontaneous motion of cavity solitons [26]. In contrast, we have recently shown that localized states propagate under translational coupling (TC) and that advection introduces different effects such as the deformation of the structure profile and optical vortex emission, i.e., optical phase singularities appear in the wake of the drifting structure [27].

The aim of this study is to characterize qualitatively the effects of TC on the dynamics of LSs. We focus on the deformation and instabilities undergone by the drifting structures. By TC we mean the dynamics of the physical quantities that describe the system at position $\vec{r}$ at a given time t depend on the physical quantities at the position $\vec{r}+\vec{L}$ at the same time t, where $\vec{L}$ is the parameter that characterizes the TC. Theoretically, based on a prototypical model of localized states modified with TC, we show that translational-type coupling modifies these states, which become deformed and propagative, also exhibiting different instabilities. Note that here we do not consider drift instabilities, which emerge

through marginal modes from the spontaneous symmetry breaking of an $x \to -x$ invariant structure in an $x \to -x$ invariant system. Indeed, TC cannot induce a drift instability since it breaks the required symmetry.

These theoretical results are compared with those obtained in a liquid crystal light-valve experiment with a mirror tilt in the feedback loop. We characterize analytically and numerically the dynamical behaviors, finding a good qualitative agreement with the experimental observations.

The paper is organized as follows. A description of the experimental setup and the procedures used in the characterization of the localized structure dynamics under TC are presented in Sec. II A. In Sec. II B numerical simulations of the full model for the light valve with TC are analyzed. A linear stability analysis of the model is presented in Sec. II C. In Sec. III we introduce a one-dimensional prototype model, which allows us to highlight the universal nature of the studied phenomenon and permits us to characterize the different mechanisms leading to the destabilization of dissipative localized states under the influence of TC. In Sec. V we extend the model to two space dimensions. Finally, a summary is presented in Sec. VI.

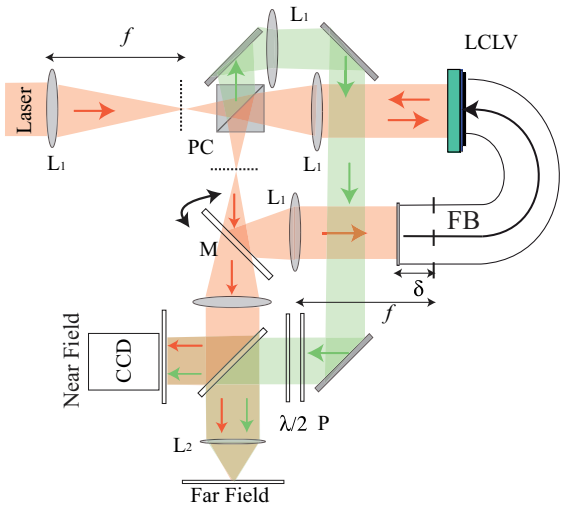

FIG. 1. (Color online) Experimental setup: FB, optical fiber bundle; L_1 and L_2, lenses; PC, polarizing cube splitter; a partially reflecting mirror deflects part of the beam to the CCD camera for detection; P, polarizer; $\lambda/2$, half-wave plate controls the polarization and intensity of the reference beam (see details in Ref. [27]).

II. LOCALIZED STRUCTURE DYNAMICS IN A LIGHT VALVE UNDER TRANSLATIONAL COUPLING

A. Experimental setup and observations

To study the effect of nonlocal coupling of the translational type on LSs, we consider a liquid crystal light valve (LCLV) inserted in an optical feedback loop [28]. The LCLV consists of a thin film of nematic liquid crystals, 15 μm thick, interposed between a glass plate and a photoconductive material over which a dielectric mirror is deposited. The confining surfaces of the cell are treated for a planar anchoring of the liquid crystal molecules (with the nematic director $\vec{n}$ parallel to the walls) [29]. Transparent electrodes deposited over the cell walls allow us to apply an external voltage V_0 across the liquid crystal layer, which is illuminated by an expanded He-Ne laser beam, $\lambda = 632.8$ nm, linearly polarized along the vertical direction. Molecules tend to orient along the direction of the applied electric field, which in turn changes locally, and dynamically, by following the illumination distribution present on the photoconductive wall of the cell. When liquid crystal molecules reorient, because of their birefringence, they induce a change of the refractive index [30]. Thus the LCLV acts as a Kerr medium, providing for the reflected beam a phase variation $\varphi = kdn_2 I_w$ proportional to the intensity I_w of the beam incoming on its photoconductive side. Here d is the thickness of the nematic layer, $k = 2\pi/\lambda$ is the optical wave number, and n_2 is the equivalent nonlinear coefficient of the LC. Once it passes through the liquid crystal, the beam is reflected back by the dielectric mirror on the rear side of the valve and sent in the feedback loop. An optical fiber bundle is used to close the loop and redirect the beam back to the photoconductive side of the LCLV. The nematic director is oriented at 45° and the polarizing cube splitter introduces polarization interference between the ordinary and extraordinary waves, a condition ensuring the bistability between differently orientated states of the liquid crystal [31].

To generate the nonlocal TC we introduce a mirror tilt in the optical feedback loop. That generates an image on the rear side of the LCLV with a displacement $\vec{L}$. For example, for a mirror tilt of exactly 45° there is no local effect of drift: $\vec{L} = \vec{0}$. Changes to this angle in either direction generate a TC. A schematic diagram of the experiment is displayed in Fig. 1. A reference beam is used to realize a Mach-Zehnder-type interferometer, which allows visualizing the optical phase. More details on the interferometer and phase features can be found in Ref. [27].

Previous studies of translational effects in the LCLV experiment have evidenced secondary instabilities of patterns [32,33] such as transitions from hexagons to stripes and from squares to zigzag [34]. More recently, it has been shown that drifting LSs can be guided by using a spatial light modulator [35]. Recently we reported in Ref. [27] the drift-induced asymmetrical deformation of LSs and the associated emission of vortices. When a translational effect is introduced in the experiment by tilting the mirror at the entrance of the feedback loop, localized states start to drift along the direction of the mirror displacement. The motion of a single LS is shown in Fig. 2, where successive experimental snapshots with interference fringe patterns are displayed with a time separation of 1.07 s. Here the drifting direction x is marked by an arrow. After the initial transient acceleration induced by the mirror tilt, the LS acquires a constant speed, as indicated by the dotted line. During the first stages of the advection, the structure loses its round shape and undergoes an asymmetrical deformation developing a large tail in its wake. The fourth panel of Fig. 2 shows a profile of a moving structure without fringes. The symmetry breaking is accompanied by the emission of pairs of optical vortices, appearing as dislocations in the interference pattern [27].

The inclination of the mirror induces the breakdown of reflection symmetry, favoring one direction, which we have denoted x. Then LSs are deformed and propagate in this

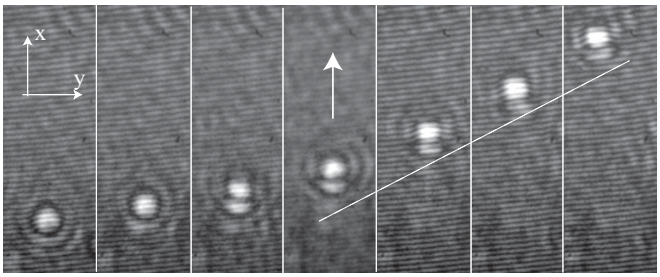

FIG. 2. Successive experimental snapshots (with a time separation of 1.07 s) showing an optical LS drifting along the x direction; the advection occurs after tilting the mirror M at the entrance of the feedback loop.

direction, as illustrated in Fig. 3. The TC induces a hump in the rear zone of the LS [see Figs. 3(a) and 3(b)]. It is important to note that increasing the displacement L increases the height of the hump. As we shall see later, the formation of the hump is a consequence of the translational nonlinear coupling of this system.

B. Numerical simulations of the LCLV model with translational coupling

To confirm the experimental observations we have performed numerical simulations of the full model for the LCLV with displaced optical feedback. The model consists in an equation for the average tilt angle $\theta(\vec{r},t)$ of the LC molecules [31]

$$\frac{2}{\pi}(\tau\partial_t\theta - l^2\nabla_\perp^2\theta + \theta) = 1 - \sqrt{\frac{V_{\mathrm{FT}}}{\Gamma V_0 + \alpha I_w(x+L,y)}}, \qquad (1)$$

where $\tau = 30$ ms and $l = 30\ \mu$m are the LC response time and electrical coherence length, respectively; $\nabla_\perp^2$ is the transverse Laplacian; V_{FT} is the Fréedericksz transition voltage; Γ is the transfer function of the equivalent electric circuit of the LCLV; V_0 is the applied voltage; α is a coefficient accounting for the response of the photoconductor, L is the translation of the feedback beam, which we will call a displacement parameter; and I_w is the intensity on the photoconductor, which has the form

$$I_w(\theta(\vec{r},t)) = \frac{I_{\mathrm{in}}}{4}\left|e^{i\delta\nabla_\perp^2/2k}\left(e^{-i\beta\cos^2\theta} - 1\right)\right|^2, \qquad (2)$$

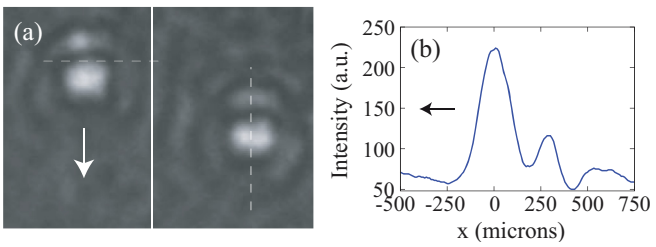

FIG. 3. (Color online) (a) Experimental snapshots of a propagating LS; the dashed line in the right panel shows the location from where the corresponding one-dimensional profile is extracted. This is shown in (b).

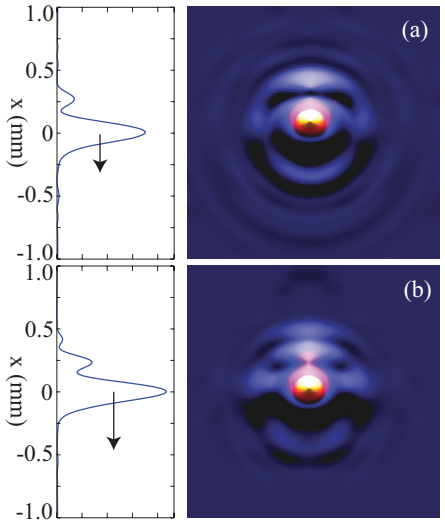

FIG. 4. (Color online) Numerical intensity profiles of a drifting localized structure obtaining from model (1): (a) $L = 126\ \mu$m and (b) $L = 182\ \mu$m; the corresponding one-dimensional profiles along the advection direction x are shown on the left.

with δ the free propagation length, $k = 2\pi/\lambda$ the optical wave number, and $\beta\cos^2\theta$ the phase shift acquired by the light when passing through the LC layer; $\beta = 4\pi\Delta n d/\lambda$, $\Delta n = 0.2$ is the LC birefringence, and d is the thickness the LC layer. The electric field at the exit of the LC layer is $E_{\mathrm{in}}(e^{-i\beta\cos^2\theta} - 1)$, where E_{in} is the input field and $I_{\mathrm{in}} = |E_{\mathrm{in}}|^2$. Numerical integrations of Eq. (1) are made under periodic boundary conditions and by using a pseudospectral method, for which the spatial derivatives and the diffraction operator are solved in Fourier space, whereas the temporal evolution is calculated with an adaptive Runge-Kutta algorithm. In the bistable regime a single LS is generated by applying a Gaussian pulse inducing a local perturbation and then a translation L of the feedback intensity I_w is introduced.

Figure 4 shows a set of numerical results for the parameters $\delta = -16$ cm, $\alpha I_{\mathrm{in}} = 1.2$, and $V_0 = 12.9$ V, giving LSs with a diameter of $D = 450\ \mu$m. The range of L for which the advection regime exists is in between 30 and 250 μm. The respective numerical intensity profiles show how the initially axisymmetric LS [$L = 0$, Fig. 4(a)] is deformed during the advection. For relatively small translations [$L = 126\ \mu$m, Fig. 4(b)], the profile is slightly deformed, with wavelets visible behind the structure. For larger drifts [$L = 182\ \mu$m, Fig. 4(c)], the deformation becomes more important, with the amplitude of the principal and secondary maxima increasing and a large wake developing behind the structure. Linear intensity profiles along the drift direction are displayed at the left column of Fig. 4.

In addition, we have numerically calculated the speed v_d of LSs as a function of the displacement L. The results are plotted in Fig. 5, where we see that the speed exhibits a linear behavior as a function of the displacement. This behavior is in qualitative agreement with the experimental observations. In the experiment it is difficult to precisely measure the displacement and speed of the LSs because of the mirror tilt procedure that introduces an initial uncertainty

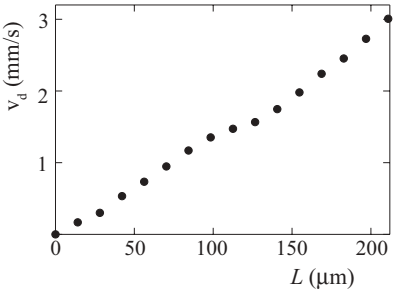

FIG. 5. Numerically calculated localized structure advection velocity v_d vs the translation L; $\delta = -16$ cm.

on both quantities. The linear behavior of v_d versus L could nevertheless be verified qualitatively by measuring after the early stages of the process the slope of the spatiotemporal plots associated with the LS dynamics.

C. Linear stability analysis of the LCLV model

In order to develop a qualitative insight into the TC induced advection regime, we perform a linear stability analysis of the LCLV model [Eqs. (1) and (2)] for $L \neq 0$. If θ_0 is a homogeneous stationary solution, we take the ansatz $\theta = \theta_0 + \varepsilon\theta_1$, with θ_1 the perturbation satisfying $\partial_t\theta_1 = \sigma t\theta_1$, and $\nabla_\perp^2\theta_1 = -q^2\theta_1$, $\varepsilon \ll 1$, and q the wave number describing the spatially periodic perturbation. By substituting the perturbed solution into Eqs. (1) and (2) and by taking, without loss of generality, the displacement in the x direction, we obtain the dispersion relation [36]

$$\sigma = -q^2 - 1 - \chi e^{iq_x L}\cos(\Lambda q^2 + \varphi_0/2), \tag{3}$$

where

$$\chi = -\frac{\pi}{4}\frac{\alpha I_{\text{in}}\beta A\sqrt{\Gamma V_{\text{FT}}}\sin 2\theta_0}{(\Gamma V_0 + \alpha I_{\text{in}}A^2)^{3/2}},$$

with $\beta = 2k(n_e - n_o)d$, where n_e and n_o are, respectively, the extraordinary and ordinary refractive indices of the liquid crystal, $A = \sqrt{(1/2)(1-\cos\varphi_0)}$, $\varphi_0 = \beta\cos^2\theta_0$, $\Lambda = -\delta/2kl^2$, $t \to \tau t$, $x \to lx$, $y \to ly$, and $q^2 = q_x^2 + q_y^2$.

Both $\text{Re}(\sigma)$ and $\text{Im}(\sigma)$ have an oscillatory behavior as a function of q. The mode associated with the maximum of $\text{Re}(\sigma) > 0$ defines a critical wave number q_c, whereas the mode corresponding to the maximum of $\text{Im}(\sigma)$ defines a critical frequency Ω_c. In this analysis, one could consider qualitatively that a LS is a small perturbation propagating at the phase velocity of the linear dispersion relation. The phase velocity can then be constructed as $v = \Omega_c/q_c$ and calculated as a function of the displacement L. The result is plotted in Fig. 6, showing a linear behavior of v on a long range of L. While a direct comparison with the LS propagation speed (Fig. 5) cannot be made, Fig. 6 provides a qualitative basis to evaluate the behavior of the velocity at which a small perturbation of the homogeneous state would propagate under the effect of translational coupling.

Figure 5, which illustrates the speed v_d of LS propagation as a function of L, shows a linear behavior for small displacements. However, for large L the LSs undergo secondary instabilities. The derivation of these instabilities from model (1) is a complex task. A simple nonlocal model is proposed in the following section, which, as we will see, allows us to catch the essential phenomenon of the LS destabilization as well as to calculate analytically the propagation speed.

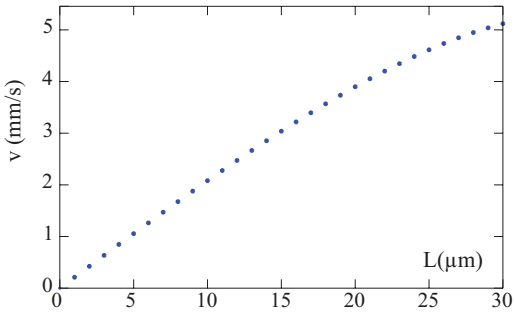

FIG. 6. (Color online) Phase velocity v at which a small perturbation of the homogeneous state would propagate under the effect of translational coupling versus the spatial displacement L.

III. SIMPLE MODEL DESCRIBING TRANSLATIONAL COUPLING IN ONE-DIMENSIONAL SYSTEMS

Numerical simulations using the phenomenological model (1) show quite good agreement with the experimental observations. However, this is an extremely complex model to realize analytical studies that can help us understand the dynamics of LS under the TC. In order to reveal the existence conditions, stability properties, and dynamical evolution of the localized states under the effect of TC, we consider the generalized Swift-Hohenberg model with TC

$$\begin{aligned}\partial_t u(x,t) = {} & \eta + \epsilon u(x+L,t) - u^3(x+L,t) \\ & - v\partial_{xx}u(x,t) - \partial_{xxxx}u(x,t),\end{aligned} \tag{4}$$

where $u(x,t)$ is a scalar field corresponding to the order parameter, evaluated at position x and time t, ϵ is the bifurcation parameter, η accounts for the asymmetry between the two stable homogeneous states, v is related to nearest-neighbor coupling [when it is negative (positive) it quantifies the diffusion (antidiffusion) coefficient], and L is the displacement that rules the TC. The generalized Swift-Hohenberg model is here chosen not only because it is the prototypical model for the emergence of stationary patterns and localized structures [2,3] but also because a generalized version including nonvariational terms (Lifshitz normal form) was previously derived for the LCLV system [31]. For the sake of clarity, we consider here the simplest scalar version, which allows us to account for localized structures and translational coupling: It is the minimal scalar model displaying localized structures and it has been derived in different contexts such as fluids, chemical reactions, population dynamics, biological models of neurons, and optical systems [2,3,37]. One of the main ingredients exhibited by the model is the possible coexistence of a pattern and a uniform state, which allows the existence of stable localized structures. This is indeed the case for the LCLV experiment, which shows multistability, a spatial instability giving rise to patterns, localized structures, and homogeneous states.

In the case of $L = \eta = 0$, the Eq. (4) corresponds to the Swift-Hohenberg model [3]. It was introduced to explain the emergence of patterns in one-dimensional nonequilibrium

systems, which was proposed in the context of Rayleigh-Bénard convection [38]. It is worth noting that for $L = 0$, the above model is local, that is, the immediate temporal evolution of the field $u(x,t)$ is determined by itself and its immediate spatial surroundings. In the case $\eta \neq 0$ the model (4) is called *the generalized Swift-Hohenberg equation*. Originally, this model was proposed to explain the appearance of LSs in optical bistability [39]. Subsequently, this model has become the prototypical model to describe the emergence of patterns and localized dissipative states. Here we consider $L \neq 0$. Translational coupling in the LCLV has simultaneously linear and nonlinear effects; for this reason, we have considered the prototypical model (4) with linear and nonlinear TC. The TC favors one direction; consequently, it breaks the reflection (rotational) symmetry of the original one-dimensional (two-dimensional) Swift-Hohenberg equation.

It is well known that for certain values of the parameters, the generalized Swift-Hohenberg equation exhibits localized states [39]. Figure 7 shows the parameter space where the smallest (one-cell) propagative LS is stable in the generalized Swift-Hohenberg equation with TC ($L = 0.8$). It is noteworthy that the motionless localized states for the generalized Swift-Hohenberg equation ($L = 0$) exist in a very similar area in the

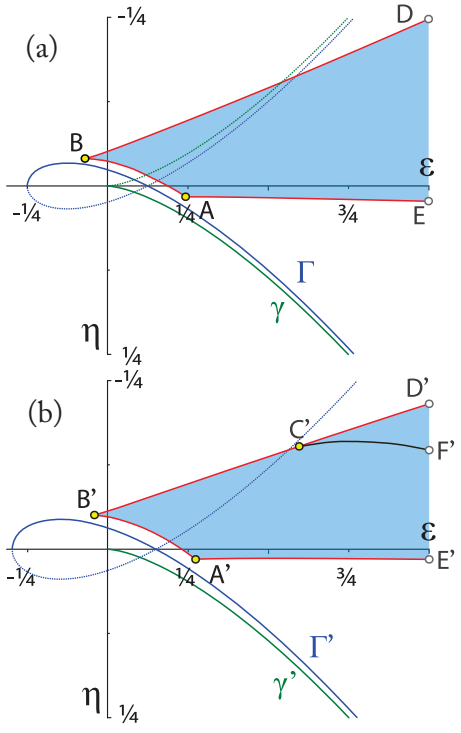

FIG. 7. (Color online) Bifurcation diagram in the $\{\epsilon,\eta\}$ space ($\nu = 1$) of the Swift-Hohenberg equation (a) without ($L = 0.0$) and (b) with TC ($L = 0.8$). The γ (or γ') curve separates the region of coexistence of uniform states. Below this curve there is only one steady state, which we have denoted by u_0. Above the γ (γ') curve the system exhibits three uniform states, two stable and one unstable. The Γ (or Γ') curve accounts for the spatial instability of the state u_0. In the shaded region $\overline{ABCD}$ ($\overline{A'B'C'D'}$) the smallest (one-cell) localized structure supported on the lower homogeneous state is stable (and propagates). For $L = 0.8$, in the region $\overline{C'D'F'}$ the localized state moves in the direction opposite to the TC.

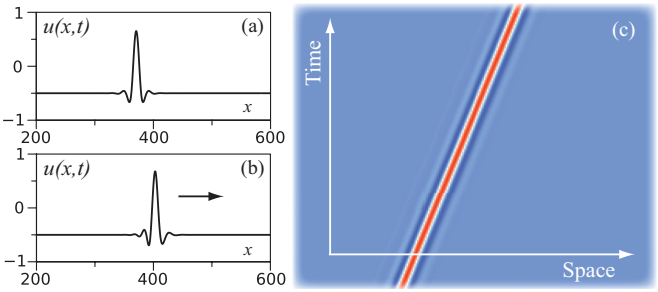

FIG. 8. (Color online) The LSs observed in the Swift-Hohenberg model with translational coupling by $\epsilon = 0.17$, $\eta = -0.04$, and $\nu = 1.00$: (a) $L = 0$ and (b) $L = 0.8$. (c) Spatiotemporal evolution of the LS with $L = 0.8$.

parameter space shown in Fig. 7 [40]. Despite the simplicity of the Swift-Hohenberg equation, analytical expressions of localized states are unknown.

To study Eq. (4) numerically, we have considered a Runge-Kutta scheme of order 4 for the temporal integration and finite differences to compute spatial derivatives over a grid of equally spaced points $\{x_k\}_{k=1}^{n}$. Since L is a continuous parameter, in order to study bifurcations one needs to evaluate the field u at an arbitrary point $y = x + L$, not necessarily in the grid. To do so, we have interpolated the value of $u(y,t)$ from the nearest five points in the grid by considering a fourth-order polynomial. Numerical simulations of Swift-Hohenberg equation with TC ($L \neq 0$) reveal that the localized states persist in this model. Figure 8 shows the smallest LS in model (4) with translational coupling for $L = 0$ [Fig. 8(a)] and $L = 0.8$ [Fig. 8(b)]. We observe that LSs are deformed and propagate in the direction favored by TC, as illustrated in Fig. 8(c). The deformation of localized states is consistent with experimental observations [cf. Fig. 3(b)], i.e., the rear damped oscillations are amplified in the presence of TC. Note that when the bifurcation parameter ϵ is large enough, the localized state moves backwards for L positive. This occurs more markedly when the TC only affects the linear term; in this case LSs also display an opposite behavior in their deformation. More precisely, the damped oscillations in front, not in the rear, of the localized state are amplified. The above analysis allow us to conclude that in the parameter region studied experimentally, the nonlinear TC terms are essential to explain the observed behavior.

A. Analytical determination of the speed of localized structures

It is straightforward to prove that if $u(x,t)$ is a solution to Eq. (4), then $u(-x,t)$ is a solution to the same equation with $L \to -L$. Now let us consider any propagative solution $u(x,t) = f(x - c(L)t)$, where $c(L)$ is the velocity of propagation. From the above symmetry property it follows directly that $c(-L) = -c(L)$. Hence, if the speed of such propagative state admits a Taylor expansion around $L = 0$, it can only contain odd terms. We will now deduce the value of the first term of such an expansion for a localized state (the same strategy is also valid in more spatial dimensions).

For $L = 0$ any localized state u_{LS} is static, thus for small L ($L \ll 1/\sqrt{\nu}$) we can consider the effect of TC as a perturbation over such a state. In this limit we can use the approximation

$u(x+L,t) \approx u(x,t) + L\partial_x u(x,t) + O(L^2)$. Equation (4) becomes (the *nonlinear convective Swift-Hohenberg equation*)

$$\partial_t u = \eta + \epsilon u(x,t) - u^3 - \nu\partial_{xx}u - \partial_{xxxx}u + L(\epsilon - 3u(x,t)^2)\partial_x u. \quad (5)$$

To compute the velocity of the LS, we consider the ansatz

$$u(x,t) \equiv u_{\rm LS}(x - x_0(t)) + W(x,x_0), \quad (6)$$

where $u_{\rm LS}(x)$ is any LS of the generalized Swift-Hohenberg equation ($L = 0$), x_0 stands for its position, corresponding to the position of its maximum, and W is a correction function of $O(L)$ that accounts for the deformations suffered by the solution. To account for the drift effect of TC, we have promoted the continuous parameter x_0 to a function of time. In the limit L tending to zero, x_0 becomes a constant and W converges to zero. Introducing the above ansatz in Eq. (5) and linearizing in W we obtain

$$\mathcal{L}W = \dot{x}_0\partial_x u_{\rm LS} + L(\epsilon - 3u_{\rm LS})\partial_x u_{\rm LS}, \quad (7)$$

where $\mathcal{L}$ is a linear operator given by

$$\mathcal{L} = \epsilon - 3u_{\rm LS}^2 - \nu\partial_{xx} - \partial_{xxxx}.$$

Introducing the inner product

$$\langle f(x)|g(x)\rangle = \int_{-\infty}^{\infty} f(x)g(x)dx, \quad (8)$$

the linear operator $\mathcal{L}$ is self-adjoint. In order to have a solution for the linear equation (7), we apply the solvability condition or Fredholm alternative [2]. Thus we obtain the following relationship for the speed of a LS:

$$\dot{x}_0 = L\left(3\frac{\langle u_{\rm LS}^2|(\partial_x u_{\rm LS})^2\rangle}{\langle\partial_x u_{\rm LS}|\partial_x u_{\rm LS}\rangle} - \epsilon\right) + O(L^3). \quad (9)$$

Therefore, in this approximation, we find that the speed of propagation of the LS is linear with L. Expression (9) helps us understand the role of linear and nonlinear TC. Since the first and second terms on the right-hand side are

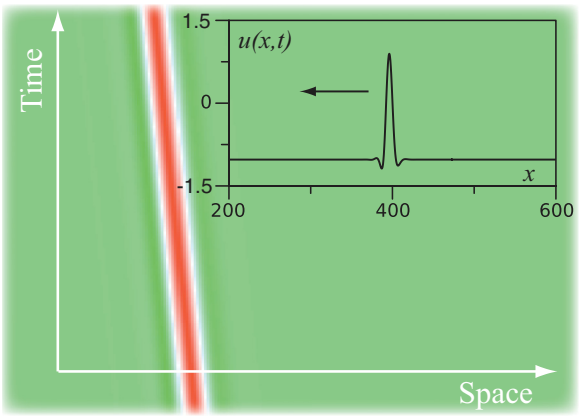

FIG. 9. (Color online) The LS moving in the direction opposite to the displacement, obtained for the Swift-Hohenberg model with translational coupling. Here $\epsilon = 0.85$, $\eta = -0.2$, $\nu = 1.00$, and $L = 0.8$.

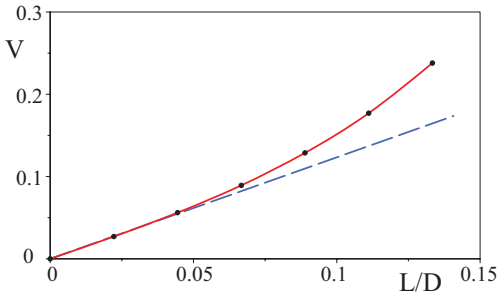

FIG. 10. (Color online) Numerical evaluation of the speed of the smallest localized state in the Swift-Hohenberg model with TC, as a function of L/D, where $D = 10.798$ is the characteristic size of the LS at $L = 0$. Except for L we fix all parameters: $\epsilon = 0.6$, $\eta = -0.04$, and $\nu = 1.00$. The solid curve was obtained with a spatial discretization step $dx = 0.2$. The dashed curve is the linear theoretical prediction, whose coefficient was numerically evaluated for $dx = 0.1$.

the result of nonlinear and linear TC, respectively, for small ϵ LSs propagate along the direction of displacement and for large enough ϵ they do it in the opposite direction. Figure 9 shows a LS moving in the direction opposite to displacement ($\epsilon = 0.85$). Such backwards propagating states are observed in the $\overline{D'C'F'}$ region shown in Fig. 7(b).

We have measured the propagation speed of LSs exhibited by the model numerically (4). Figure 10 depicts this speed as a function of the displacement parameter L. We note that for small displacements compared to the size of the LS the formula (19) consistently describes the observed dynamics (see Fig. 10). However, for larger displacements, the speed is governed by nonlinear corrections in L (cubic, quintic, and so forth). Then the measured speed of the localized state systematically moves away from the theoretical linear prediction. However, both the linear stability analysis and numerical simulations of the LCLV model mainly present a linear regime as a function of L (see Figs. 5 and 6). As we will see later, the linear regime is wider in two dimensions.

Remarkably, the above analysis allows us to recognize, by simply inspecting the direction of the LS advection with respect to the deformation, that the TCs in the experiment are mainly dominated by the nonlinear coupling induced by the optical feedback.

IV. MECHANISMS OF DESTABILIZATION OF PROPAGATIVE LOCALIZED STRUCTURES

When increasing the displacement parameter L, or by changing the parameters $\{\eta,\epsilon\}$ in model (4), LSs lose stability through different processes. In the following sections we discuss the different mechanisms of instability undergone by LSs. A bifurcation diagram is constructed for the smallest localized state (Fig. 7).

A. Saddle-node bifurcation

When one begins to decrease the asymmetry parameter η, the stable LS is modified so that the dominant peak decreases. This dynamical behavior continues until one finds a critical value of η_c, for which the LS vanishes converging

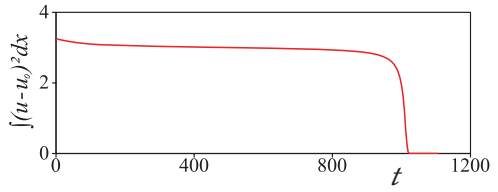

FIG. 11. (Color online) Temporal evolution of the relative norm, formula (11), considering the Swift-Hohenberg model with translational coupling $\epsilon = 0.2$, $\eta = -0.01$, $\nu = 0.3$, and $L\sqrt{\nu} = 0.458$.

to the homogeneous solution. In this process the maximum of the solution initially decays slowly and suddenly drops quickly towards the homogeneous state. For $L = 0$, the process described above occurs when one crosses the segment $\overline{BD}$ in the parameter space shown in Fig. 7(a) [$\overline{B'D'}$ for $L = 0.8$ in Fig. 7(b)]. Alternatively, this can be obtained by increasing L for certain given values of $\{\epsilon,\eta\}$. In order to characterize this process, we consider the relative norm of the LS, $N_{\rm rel}$, defined as

$$N_{\rm rel}(t) = \int_{-\infty}^{\infty} [u(x,t) - u_0]^2 dx, \tag{10}$$

where u_0 stands for the uniform state that supports the LS. Figure 11 shows the temporal evolution of the relative norm of a LS. Clearly, this graphic shows that for a long time the localized state almost maintains its relative norm, which decreases exponentially, and then it suddenly drops until it vanishes: The system displays the uniform state u_0 as equilibrium. This type of behavior of the sudden disappearance of an equilibrium is typical of a saddle-node bifurcation [41] and is commonly referred to as *ghost* or *ruin* [42], that is, a metastable localized state remains for a long time until it starts to decrease and suddenly disappears. These long transients are characterized by a residence time diverging T with a power law $1/2$ as one approaches the saddle-node bifurcation [42]. We have considered the following strategy to study these dynamical transients exhibited by the unstable localized state. We set all the parameters of the model (4) at a suitable point and begin to decrease the displacement parameter L. For each L we calculate the cumulative relative norm

$$A(L) = \int_{t_0}^{\infty} N_{\rm rel}(t) dt. \tag{11}$$

As a result of the mean value theorem, A is proportional to the residence time near the bifurcation. Theory shows that this time diverges with a power law $1/2$ near a critical value L_c; then the cumulative norm A must diverge with the same law. Figure 12 shows the cumulative norm $A(L)$ measured near the bifurcation (4) and the numerical fit considering groups of five points

$$A = A_0 \left(\frac{L}{L_c} - 1 \right)^{\alpha}, \tag{12}$$

where $\alpha = 0.500\,03$, $L_c\sqrt{\nu} = 0.451\,220$, and $A_0 = 153.8$ considering the parameters $\eta = -0.01$, $\epsilon = 0.2$, and $\nu = 0.3$. Therefore, the previous result confirms that this bifurcation corresponds to a saddle node. Notice that when considering

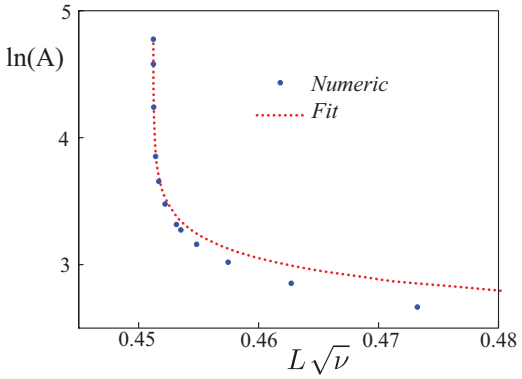

FIG. 12. (Color online) Cumulative area as a function of the displacement parameter L. The dots represent the values obtained numerically from the model (4) for $\epsilon = 0.2$, $\eta = -0.01$, and $\nu = 0.3$. The dashed curve is obtained by using the fitting formula (12) and by considering the first five points.

more distant points the power law changes and even ceases to be a power law because it is only valid for a region near the critical value L_c. Experimentally, we observe qualitatively that the localized states disappear through this mechanism; however, a study to provide a detailed characterization of the process is an experimentally complex task.

B. Pattern formation instability

In contrast, by increasing the displacement parameter L or by increasing η for small ϵ, we observe that the amplitude of spatial oscillations of the rear tail of the smallest propagative LSs (also other LSs) begin to grow, giving rise to the emergence of patterns. Figure 13 depicts the process of the pattern emergence from an unstable localized state. The growth of spatial damped oscillations of the localized state is a signal that the uniform solution that supports the LS is close to becoming unstable. Indeed, as one can see in Fig. 7, the above process occurs when one crosses the $\overline{AB}$ ($\overline{A'B'}$) curve, which runs close and nearly parallel to the Γ (Γ') curve.

To elucidate this mechanism, let us denote by u_0 the homogeneous state towards which the LS converges at infinity; it satisfies the relation

$$0 = \eta + \epsilon u_0 - u_0^3.$$

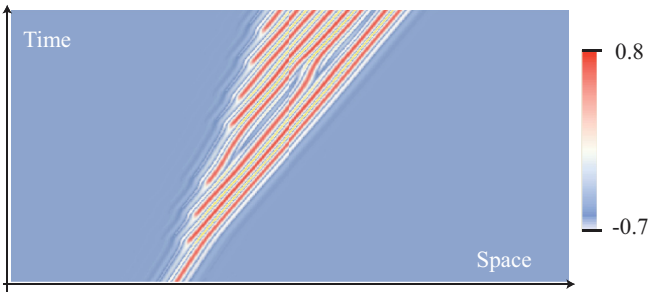

FIG. 13. (Color online) Spatiotemporal diagram showing the evolution of an unstable localized structure that generates the appearance of patterns in the model (4); $\epsilon = 0.18$, $\eta = -0.04$, $\nu = 1.00$, and $L = 1.2$.

To study the stability of u_0, we introduce the following ansatz $u = u_0 + ve^{\lambda(k)t+ikx}$ in Eq. (4), where v is a small complex number and the real part of $\lambda(k)$ stands for the growth rate of the harmonic mode with wave number k. After straightforward calculations we obtain the relation

$$\lambda = \left(\epsilon - 3u_0^2\right) e^{iLk} + \nu k^2 - k^4. \tag{13}$$

Then, if the real part of λ is positive (negative), the solution u_0 is unstable (stable). Thus the instability curve might be obtained by determining the maxima of λ as a function of k $[k_c(L,\epsilon,\nu,\eta)]$ and then by imposing that the real part of λ is equal to zero at these points. This procedure creates a relationship between k_c (critical wave number), L, and the other parameters (ϵ,ν,η), which represents *the instability curve*. Because of the complexity of analytical expressions for u_0, we introduce the auxiliary parameters

$$\chi \equiv \left(\epsilon - 3u_0^2\right)/\nu^2, \quad \psi \equiv Lk, \tag{14}$$

the first representing the control parameter and the second accounting for the length of the translational coupling.

After straightforward calculations we obtain the transcendental relationship

$$\frac{\chi}{2}[\psi \sin(\psi) + 4\cos(\psi)]^2 = -\psi \sin(\psi) - 2\cos(\psi), \tag{15}$$

which is plotted in Fig. 14. The solid curve represents the relationship (15) solved for L_c. The top (bottom) of this curve represents the region of parameter space where the uniform state u_0 is unstable (stable). To develop an approximate analytical expression for the instability curve, we can first consider the limits $\chi \to -\infty$ and $\chi \to -1/4$. The latter case corresponds to the limit $L \to 0$. In both limits one can obtain simple analytical expressions. From these expressions and by using the Padé approximant method [43], we can interpolate the transcendental equation (15) and obtain

$$\psi = \frac{c_1 z + c_2 z^2 + c_3 z^3}{1 + d_1 z + d_2 z^2 + d_3 z^3}, \tag{16}$$

where $z = \sqrt{-(1/4+\chi)}$, $c_1 = 2.83$, $c_2 = 7.02$, $c_3 = 8.60$, $d_1 = 2.48$, $d_2 = 4.20$, and $d_3 = 4.20$. Thus the critical wave number has the expression

$$k_c = \tfrac{1}{2}\sqrt{\nu[1 + \sqrt{1 + (1+4z^2)\psi \sin\psi}]}.$$

One noteworthy advantage of the Padé approximant method is that it provides simple expressions with which one can perform analytical calculations. In Fig. 14 the dashed line shows the results obtained by using the formula based on the Padé approximant method (16). The relative difference between the areas below the curves obtained using formulas (15) and (16) is $10^{-5}\%$. Therefore, we conclude that the Padé method allows us to have a correct and manipulable approximation for the instability curve, except near its maximum, where it slightly underestimates the value of L_c. It is easy to prove analytically that this maximum occurs exactly at $L = L_c^*\sqrt{\nu} \equiv \pi/2$ and also $\chi = \chi^* \equiv -4/\pi$ and $k_c = k_c^* \equiv 1$. For any value of L above L_c^*, the homogeneous state is spatially unstable and no LS can be stable. Numerical simulations show that when one crosses the instability curve $\overline{AB}$ or $\overline{A'B'}$ (see Fig. 7), the localized state becomes unstable and from it a pattern solution is engendered, as illustrated in Fig. 13.

C. Front emission

For a fixed displacement parameter L, positive and large ϵ, and negative η, we observed a different mechanism of destabilization of the dissipative LSs. The localized state is destabilized through the emission of two counterpropagative fronts. Because of the TC, while the forward front propagates at a speed close to zero, the rear front propagates in the opposite direction and with a higher speed. Figure 15 shows the space-time diagram of this process. The above process occurs when one crosses the $\overline{AE}$ ($\overline{A'E'}$) curve in the space of parameters illustrated in Fig. 7. These fronts appear because the upper homogeneous state is more stable than the lower one. Thus, through the emission of a couple of fronts, the system arrives at the most stable state.

Front dynamics in the LCLV experiment has been previously characterized both for homogenous liquid crystal reorientation [44,45] and in the pinning-depinning regime under spatially periodic forcing [46,47].

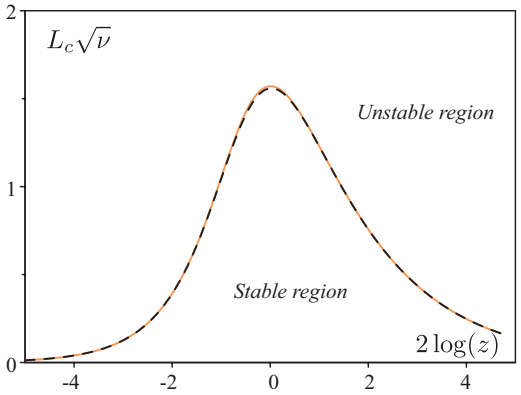

FIG. 14. (Color online) Spatial instability curve for the uniform state u_0, L versus $2\ln(z)$, with $z \equiv [-(1/4+\chi)]^{1/2}$. The solid and dashed curves represent, respectively, the transcendental relation (15) and a Padé approximation (16).

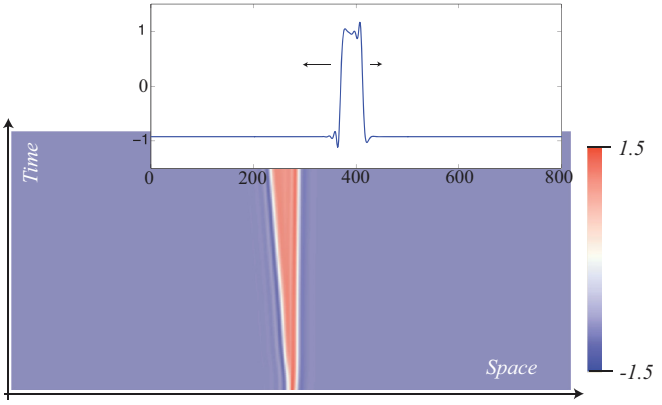

FIG. 15. (Color online) Spatiotemporal diagram showing the front emission: An unstable LS generates the emission of two counterpropagative fronts in the model (4); $\epsilon = 0.9$, $\eta = 0.04$, $\nu = 1.00$, and $L = 0.76$.

V. GENERALIZATION OF THE MODEL TO TWO-DIMENSIONAL EXTENDED SYSTEMS

The one-dimensional model (4) allows us to characterize the universal behavior of the LS under the influence of TC. However, experimental observations are performed in a two-dimensional framework. In order to compare the results of the preceding sections, we consider here a generalization of the model in two space dimensions

$$\partial_t u(\vec{r},t) = \eta + \epsilon u(\vec{r}+\vec{L},t) - u^3(\vec{r}+\vec{L},t) - \nu\nabla^2 u - \nabla^4 u, \tag{17}$$

where $\vec{r}(x,y)$ represents the position vector, $\vec{L}$ stands for the displacement vector, and $\nabla^2 = \partial_{xx} + \partial_{yy}$ is the Laplacian operator. Henceforth, for the sake of simplicity, we consider $\vec{L} = L_0\hat{x}$ describing, without loss of generality, the translation in a given direction. For $L_0 = 0$, it is well known that the above model exhibits a LS [39]. When we consider the effect of TC ($L_0 \neq 0$), the localized state is deformed and becomes propagative along the direction of the TC. This deformation is characterized by an amplification of the rear spatial oscillations, accompanied by the loss of rotational symmetry of the solution. Indeed, the LS profile becomes elliptical, favoring the direction of TC, which is consistent with the experimental observations (see Fig. 3). Figure 16(a) illustrates the LS obtained for Eq. (17), which shows good qualitative agreement with those observed experimentally (cf. Fig. 3) and numerically using the LCLV model (1).

By fixing the parameters to constant values and increasing L_0, we study the speed of propagation of localized states. Figure 16(b) shows this speed as a function of the displacement parameter L_0. For small L_0, we note that the speed has a linear behavior in a wider region than in the one-dimensional case. For large L_0, the speed exhibits a nonlinear behavior,

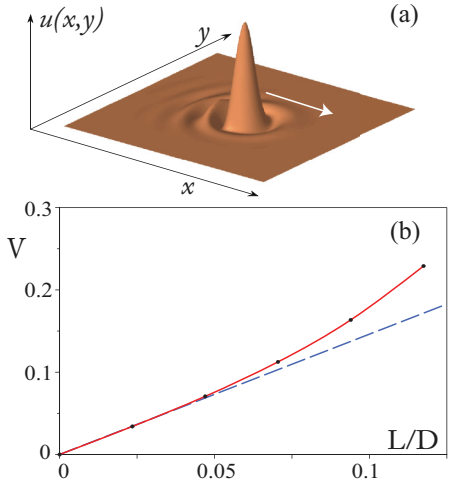

FIG. 16. (Color online) (a) Propagative LSs obtained from the model (17) for $\epsilon = 0.5$, $\eta = -0.05$, $\nu = 1.00$, and $L_0 = 1.5$. Rear oscillations are clearly amplified, breaking the rotational symmetry present in the case $L = 0$. (b) Speed of LSs as a function of L/D, where $D = 12.112$ is the size of the LS at $L = 0$. Except for L we fix all parameters: $\epsilon = 0.005$, $\eta = -6e-5$, and $\nu = 0.1$. The solid curve represents numerical measurements of the velocity and the dashed line is the linear theoretical prediction.

characterized by a significant increase of its value. In order to study analytically the speed evolution, we can adopt the same strategy as used in Sec. III A, that is, we consider the ansatz

$$u(\vec{r},t) \equiv u_{\rm LS}(\vec{r} - \vec{r}_0(t)) + w(\vec{r},\vec{r}_0(t)). \tag{18}$$

Introducing this ansatz in Eq. (17) and performing the same procedure as that presented in Sec. III A, we obtain

$$\dot{\vec{r}}_0 \cdot \hat{x} = L\left(3\frac{\langle\langle u_{\rm LS}^2|(\partial_x u_{\rm LS})^2\rangle\rangle}{\langle\langle \partial_x u_{\rm LS}|\partial_x u_{\rm LS}\rangle\rangle} - \epsilon\right), \tag{19}$$

with

$$\langle\langle f|g\rangle\rangle \equiv \int f(x,y)g(x,y)dx\,dy.$$

From the above result we can see that the expressions for the speed in one and two dimensions are similar. The solid curve shown in Fig. 16(b) accounts for the above analytical expression, which in the linear regime exhibits good agreement with the numerical findings. This shows that in a large region of parameters one expects to observe a linear behavior of the speed as a function of the displacement parameter L_0. The result is consistent with the experimental observations and the LCLV model.

VI. CONCLUSION

In past decades scientists have dedicated much attention and effort to understanding LSs, inspired by their potential applications. By using TC, we have presented the possibility of manipulating the dissipative localized states, that is, moving them in a controlled fashion. In a light-valve experiment we have shown that under the influence of this type of coupling, dissipative localized states begin to move with constant speed and are deformed, developing a tail along the direction of coupling.

We expect this type of dynamic behavior to be common to a large class of physical systems. In fact, this is manifested in the present study, where, motivated by the experimental observations, we have considered a prototypical and general model of dissipative localized states with translational coupling. From this model we have been able to capture the main physical features of the phenomenon and to observe both numerically and analytically the same type of dynamical behavior as in the experiment and in the LCLV model.

In particular, we have shown that dissipative localized states in one dimension become unstable by three mechanisms: saddle-node bifurcation, counterpropagative front emission, and spatial instability. In the latter two cases, the disappearance of the localized state is accompanied by the emergence of complex spatiotemporal structures. In two dimensions, dissipative LSs are destabilized by mechanisms similar to those observed in one dimension. Here the emergence of patterns exhibits more complex spatiotemporal dynamics, whose characterization requires further studies.

As an important outcome of the model, we have identified a potential, and efficient, way to control or manipulate dissipative LSs. Indeed, we show that this can be achieved by introducing a time-dependent displacement vector $L(t)$, which enables one to manage and move localized states to the

most appropriate place. A relevant question is the feasibility of generating TC in diverse physical systems. In the framework of mechanical systems (fluid or elastic media), magnetic media, chemical reactions (diffusion reaction) to create, or design, a TC might be a complex task. In contrast, in optical systems TC is naturally present because of the nonlocal nature of diffraction and can be easily amplified by introducing small misalignments of the optical beams. Therefore, the study of the effect of TC for optical systems is quite relevant, although most experimental systems are designed to avoid such effects.

ACKNOWLEDGMENTS

We acknowledge financial support of the Agence Nationale de la Recherche international program, Project No. ANR-2010-INTB-402-02 (ANR-CONICYT 39), COLORS. M.G.C. is grateful for financial support from the Fondo Nacional de Desarrollo Científico y Tecnológico through Project No. 1120320 and Anillo Grant ACT127. F.d.C. acknowledges financial support from Comisión Nacional de Investigación Científica y Tecnológica by *Beca Magister Nacional*.

[1] G. Nicolis and I. Prigogine, *Self-Organization in Nonequilibrium Systems: From Dissipative Structures to Order through Fluctuations* (Wiley, New York, 1977).
[2] L. M. Pismen, *Patterns and Interfaces in Dissipative Dynamics*, Springer Series in Synergetics (Springer, Berlin, 2006).
[3] M. C. Cross and P. C. Hohenberg, Rev. Mod. Phys. **65**, 851 (1993).
[4] *Localized States in Physics: Solitons and Patterns*, edited by O. Descalzi, M. Clerc, S. Residori, and G. Assanto (Springer, Berlin, 2010).
[5] H. G. Purwins, H. U. Bodeker, and Sh. Amiranashvili, Adv. Phys. **59**, 485 (2010).
[6] T. Ackemann, W. J. Firth, and G. L. Oppo, Adv. At. Mol. Opt. Phys. **57**, 323 (2009).
[7] A. C. Newell, *Solitons in Mathematics and Physics* (Society for Industrial and Applied Mathematics, Philadelphia, 1985).
[8] M. Remoissenet *Waves Called Solitons: Concepts and Experiments* (Springer, Heidelberg, 1999).
[9] P. Coullet, Int. J. Bif. Chaos **12**, 2445 (2002).
[10] P. Coullet, C. Riera, and C. Tresser, Phys. Rev. Lett. **84**, 3069 (2000).
[11] W. van Saarloos and P. C. Hohenberg, Phys. Rev. Lett. **64**, 749 (1990).
[12] P. D. Woods and A. R. Champneys, Physica D **129**, 147 (1999).
[13] G. W. Hunt, G. J. Lord, and A. R. Champneys, Comput. Methods Appl. Mech. Eng. **170**, 239 (1999).
[14] M. G. Clerc and C. Falcon, Physica A **356**, 48 (2005).
[15] U. Bortolozzo, M. G. Clerc, C. Falcon, S. Residori, and R. Rojas, Phys. Rev. Lett. **96**, 214501 (2006).
[16] O. Thual and S. Fauve, J. Phys. (Paris) **49**, 1829 (1988); S. Fauve and O. Thual, Phys. Rev. Lett. **64**, 282 (1990).
[17] V. Hakim and Y. Pomeau, Eur. J. Mech. B Fluids Suppl. **10**, 137 (1991).
[18] S. Barland *et al*., Nature (London) **419**, 699 (2002).
[19] U. Bortolozzo and S. Residori, Phys. Rev. Lett. **96**, 037801 (2006).
[20] M. G. Clerc, F. Haudin, S. Residori, U. Bortolozzo, and R. G. Rojas, Eur. Phys. J. D **59**, 43 (2010).
[21] F. Haudin, R. G. Rojas, U. Bortolozzo, S. Residori, and M. G. Clerc, Phys. Rev. Lett. **107**, 264101 (2011).
[22] M. G. Clerc, R. G. Elías, and R. G. Rojas, Philos. Trans. R. Soc. London Ser. A **369**, 412 (2011).
[23] U. Bortolozzo, P. L. Ramazza, and S. Boccaletti, Chaos **15**, 013501 (2005).
[24] E. Caboche, F. Pedaci, P. Genevet, S. Barland, M. Giudici, J. Tredicce, G. Tissoni, and L. A. Lugiato, Phys. Rev. Lett. **102**, 163901 (2009).
[25] L. Gordillo, T. Sauma, Y. Zarate, I. Espinoza, and N. Mujica, Eur. Phys. J. D **62**, 39 (2011).
[26] M. Tlidi, A. G. Vladimirov, D. Pieroux, and D. Turaev, Phys. Rev. Lett. **103**, 103904 (2009).
[27] F. Haudin, R. G. Rojas, U. Bortolozzo, M. G. Clerc, and S. Residori, Phys. Rev. Lett. **106**, 063901 (2011).
[28] S. Residori, Phys. Rep. **416**, 201 (2005).
[29] P. G. de Gennes and J. Prost, *The Physics of Liquid Crystals*, 2nd ed. (Oxford University Press, Oxford, 1993).
[30] I. C. Khoo, *Liquid Crystals: Physical Properties and Nonlinear Optical Phenomena*, 2nd ed. (Wiley Interscience, New York, 2007).
[31] M. G. Clerc, A. Petrossian, and S. Residori, Phys. Rev. E **71**, 015205 (2005).
[32] P. L. Ramazza, S. Boccaletti, A. Giaquinta, E. Pampaloni, S. Soria, and F. T. Arecchi, Phys. Rev. A **54**, 3473 (1996).
[33] P. L. Ramazza, S. Boccaletti, A. Giaquinta, E. Pampaloni, S. Soria, and F. T. Arecchi, Phys. Rev. A **54**, 3472 (1996).
[34] P. L. Ramazza, S. Ducci, and F. T. Arecchi, Phys. Rev. Lett. **81**, 4128 (1998).
[35] C. Cleff, B. Gütlich, and C. Denz, Phys. Rev. Lett. **100**, 233902 (2008).
[36] R. Rojas, Ph.D. thesis, University of Nice-Sophia Antipolis, 2005, http://tel.archives-ouvertes.fr.
[37] G. Kozyreff and M. Tlidi, Chaos **17**, 037103 (2007).
[38] J. Swift and P. C. Hohenberg, Phys. Rev. A **15**, 319 (1977).
[39] M. Tlidi, P. Mandel, and R. Lefever, Phys. Rev. Lett. **73**, 640 (1994).
[40] P. Coullet, C. Riera, and C. Tresser, Prog. Theor. Phys. Suppl. **139**, 46 (2000).
[41] O. Descalzi, M. Argentina, and E. Tirapegui, Phys. Rev. E **67**, 015601 (2003).
[42] S. H. Strogatz, *Nonlinear Dynamics and Chaos: With Applications to Physics, Biology, Chemistry and Engineering* (Addison-Wesley, Reading, MA, 1994).
[43] G. A. Jr. Baker, in *Advances in Theoretical Physics*, edited by K. A. Brueckner, Vol. 1 (Academic, New York, 1965).
[44] M. G. Clerc, S. Residori, and C. S. Riera, Phys. Rev. E **63**, 060701(R) (2001).
[45] M. G. Clerc, T. Nagaya, A. Petrossian, S. Residori, and C. S. Riera, Eur. Phys. J. D **28**, 435 (2004).
[46] F. Haudin, R. G. Elías, R. G. Rojas, U. Bortolozzo, M. G. Clerc, and S. Residori, Phys. Rev. Lett. **103**, 128003 (2009).
[47] F. Haudin, R. G. Elías, R. G. Rojas, U. Bortolozzo, M. G. Clerc, and S. Residori, Phys. Rev. E **81**, 056203 (2010).